



Composite of methyl polysiloxane and avocado biochar as adsorbent for removal of ciprofloxacin from waters

Roberta A. Teixeira¹ · Eder C. Lima^{2,3,4} · Antônio D. Benetti¹ · Pascal S. Thue³ · Diana R. Lima⁴ · Farooq Sher⁵ · Glaydson S. dos Reis⁶ · Navid Rabiee^{7,8} · Moaaz K. Seliem⁹ · Mohamed Abatal¹⁰

Received: 23 March 2022 / Accepted: 25 May 2022 / Published online: 31 May 2022
© The Author(s), under exclusive licence to Springer-Verlag GmbH Germany, part of Springer Nature 2022

Abstract

Two carbon composite materials were prepared by mixing avocado biochar and methyl polysiloxane (MK). Firstly, MK was dissolved in ethanol, and then the biochar was added at different times. In sample 1 (R₁), the time of adding biochar was immediately after dissolving MK in ethanol, and in sample 2 (R₂), after 48 h of MK dissolved in ethanol. The samples were characterized by nitrogen adsorption/desorption measurements obtaining specific surface areas (S_{BET}) of 115 m² g⁻¹ (R₁) and 580 m² g⁻¹ (R₂). The adsorbents were further characterized using scanning electron microscopy, FTIR and Raman spectroscopy, adsorption of vapors of n-heptane and water, thermal analysis, Bohem titration, pH_{pzc}, and C H N elemental analysis. R₁ and R₂ adsorbents were employed as adsorbents to remove the antibiotic ciprofloxacin from the waters. The $t_{1/2}$ and $t_{0.95}$ based on the interpolation of Avrami fractional-order were 20.52 and 246.4 min (R₁) and 14.00 and 157.6 min (R₂), respectively. Maximum adsorption capacities (Q_{max}) based on the Liu isotherm were 10.77 (R₁) and 63.80 mg g⁻¹ (R₂) for ciprofloxacin. The thermodynamic studies showed a spontaneous and exothermic process for both samples, and the value of ΔH° is compatible with physical adsorption.

Keywords Methyl polysiloxane and biochar composite · Hydrophobic surface · Pharmaceutical adsorption · Adsorption thermodynamics · Synthetic effluents

Responsible Editor: Tito Roberto Cadaval Jr

✉ Eder C. Lima
profederlima@gmail.com; eder.lima@ufrgs.br

¹ Graduate Program in Water Resources and Environmental Sanitation, Hydraulic Research Institute (IPH), Federal University of Rio Grande Do Sul (UFRGS), Porto Alegre, RS, Brazil

² Institute of Chemistry, Federal University of Rio Grande Do Sul (UFRGS), Av. Bento Gonçalves 9500, RS, Postal Box, 15003, Porto Alegre ZIP 91501-970, Brazil

³ Graduate Program in Science of Materials (PGCIMAT), Institute of Chemistry, Federal University of Rio Grande Do Sul (UFRGS), Av. Bento Gonçalves 9500, Porto Alegre, RS ZIP 91501-970, Brazil

⁴ Metallurgical, and Materials Engineering (PPGE3M), School of Engineering, Graduate Program in Mine, Federal University of Rio Grande Do Sul (UFRGS), Av. Bento Gonçalves 9500, Porto Alegre, RS, Brazil

⁵ Department of Engineering, School of Science and Technology, Nottingham Trent University, Nottingham NG11 8NS, UK

⁶ Department of Forest Biomaterials and Technology, Swedish University of Agricultural Sciences, Biomass Technology Centre, 901 83 Umeå, Sweden

⁷ Department of Physics, Sharif University of Technology, P.O. Box 11155-9161, Tehran, Iran

⁸ School of Engineering, Macquarie University, Sydney, NSW 2109, Australia

⁹ Faculty of Earth Science, Beni-Suef University, Beni-Suef, Egypt

¹⁰ Facultad de Ingeniería, Universidad Autónoma del Carmen, C.P. 24153 Ciudad del Carmen, Mexico

Introduction

Releases of contaminants of emerging concerns (CECs) to water bodies have been a critical environmental concern in the last years (Sophia and Lima 2018) because these compounds can distress the aquatic ecosystem (Ma et al. 2022). These CECs come from the pesticides, pharmaceutical, textile, petrochemical industries, human and animal excretions, and hospital effluents (Sophia and Lima 2018). One pharmaceutical class of relevant concern to the environment is the antibiotic class, which humans and livestock frequently employ. The release of antibiotics into water bodies could generate microbial resistance (Qiu et al. 2019; Bondarczuk and Piotrowska-Seget 2019); therefore, its removal from water is relevant.

The municipal wastewater treatment plants present failures in removing antibiotics and other CECs (Wang et al. 2021b) completely. Therefore, tertiary water treatment procedures are necessary to complete the removal of CECs (Arefi-Oskoui et al. 2022; Tian et al. 2022).

The methods for treatment of antibiotic contaminated waters take place using membrane filtration (Arefi-Oskoui et al., 2022), Fenton-like advanced oxidative process (Tian et al. 2022; Yu et al. 2022), photocatalysis (Baaloudj et al., 2021), ozone treatment (Foroughi et al., 2022), plasma degradation (Li et al. 2021), and adsorption (Arif et al., 2022; de Oliveira Carvalho et al. 2019; Guellati et al. 2022; Kovtun et al. 2020; Magesh et al. 2022).

Adsorption is preferable for antibiotic-loaded wastewater treatment due to its low-initial effectuation costs, easy operation, and high adsorption effectiveness of CECs from wastewaters (Caicedo et al. 2020; dos Reis et al. 2016; Thue et al. 2020; Tomul et al. 2020; Yazidi et al. 2020; Sellaoui et al. 2021).

The most commonly employed adsorbent utilized to remove pharmaceuticals from aqueous effluents is activated carbon (de Oliveira Carvalho et al. 2019; Thue et al., 2018; Hanafy et al. 2021, Sellaoui et al. 2017, 2019) and other carbon-based adsorbents such as biochar (Tomul et al. 2020). On the other hand, different composite materials (Arif et al. 2022; Caicedo et al. 2020; dos Reis et al. 2016; Guellati et al. 2022; Khan et al. 2020; Kovtun et al. 2020; Lawal et al. 2019; Magesh et al. 2022; Thue et al. 2020; Wang et al. 2021a; Yadav et al. 2021; Yu et al. 2018, Sellaoui et al. 2022) are used as alternatives to activated carbons. In addition, adsorbents derived from polysiloxanes have been utilized to remove pharmaceuticals (dos Reis et al. 2016; Kollarahithlu and Balakrishnan 2021; Panahi et al. 2019).

Polysiloxane composite materials have some benefits as adsorbents, such as high stability at a higher temperature, better mechanical strength, no swelling (dos Reis

et al. 2016), and the facility of being chemically modified and functionalized because of the presence of free silanol groups on their surfaces (Çok and Gizli 2020). On the other hand, polysiloxane's hybrid materials are more costly adsorbents than biochar and other biomass-based materials produced from low-cost biomass precursors (Cunha et al. 2020; Lima et al. 2019a; Thue et al. 2017).

Avocado seed corresponds to approximately one-quarter of the total fruit (Leite et al. 2017). The annual production of Avocado in Brazil surpasses 240,000 tons, which will generate about 60,000 tons of avocado seed (STATISTA 2020). In addition, the preparation of activated biochar from avocado seed as an adsorbent has been reported in the literature (Leite et al. 2017, 2018; Kudo et al. 2020); however, this material presents the drawbacks of low mechanical strength.

Therefore, combining avocado seed biochar and synthetic polysiloxane material precursors and producing a new composite material seems to be a clever strategy to use a biomass-based material and polysiloxane to obtain adsorbent with mechanical strength and good sorption capacity. Furthermore, this composite material should present rigidity and elevated hydrophilic behavior, and it could be used as adsorbents for a large number of CECs.

For the first time, the production of new composite adsorbent materials is reported using avocado biochar and methyl polysiloxane (MK) at a 1:0.5 ratio. Firstly MK was dissolved in ethanol, and then the avocado biochar was added at different times. In sample 1 (R₁), the time of adding biochar was immediately after dissolving MK in ethanol, and in sample 2 (R₂), after 48 h of MK dissolved in ethanol. Subsequently, different analytical techniques fully characterized the samples R₁ and R₂. The adsorbents R₁ and R₂ were used to remove ciprofloxacin (CIP) from aqueous effluents.

This work chose ciprofloxacin (CIP) as the adsorbate because it is a broad-spectrum antibiotic largely employed for various treatments (Igwegbe et al. 2021; Sadredinamin et al. 2022). Also, it has been discovered that the toxicity of CIP present in aquatic phytoplankton and algae (Nie et al. 2013; Hagenbuch and Pinckney 2012). Therefore, the study of removing CIP antibiotic from aqueous effluents is indeed important.

Materials and methods

Reactants and solutions

In order to prepare the composite material, methylpolysiloxane (MK) was provided by Silres® MK. Ciprofloxacin (CIP, C₁₇H₁₈FN₃O₃ MM: 331.347 g mol⁻¹, CAS: 86393-32-0, Fig S1) was furnished by Merck.

A 1.00 g L⁻¹ stock solution of CIP was prepared using deionized water. The working CIP solutions were prepared by dilution of the stock solution.

Preparation of polysiloxane and biochar

The avocado biochar was prepared by carbonizing 50.0 g of avocado seed powder at 500 °C using the conditions previously described (Leite et al. 2018).

Composite adsorbents prepared from avocado biochar and MK polysiloxane were prepared following the procedure. Briefly, 5.0 g MK was dissolved in 50.0 mL ethanol, and immediately after the dissolution of MK (about 15 min), 10.0 of avocado biochar was added and 0.5 mL NH₃. The system was kept under reflux at 70 °C for 48 h. Afterward, the heating was stopped, the reactional mixture was filtered, and the product was washed with water + ethanol mixture (1:1). Finally, the product was dried at 130 °C for 12 h. This first product was called (R₁). Then, a second procedure was carried out when the avocado biochar was added after 48 h of dissolution of MK in water in the presence of NH₃ solution. In this case, the biochar was added after hydrolysis, and polycondensation of MK was already taken (R₂) before adding avocado biochar. The reactional mixture was stirred for 1 h, and then the reaction was stopped, and the final product was washed with ethanol + water (1:1) and dried at 130° for 12 h (R₂) (see Fig. S2).

Composite characterizations

R₁ and R₂ composite adsorbents (< 250 μm) were used in the batch contact adsorption to decrease diffusion limitation when a larger particle diameter is employed.

Nitrogen adsorption/desorption isotherm analysis (Tristar 3000 apparatus, Micrometrics Instrument Corp.) was carried out to determine the surface area (BET method) (Thommes et al. 2015) and the volume of pores (by DFT method) (Jagiello and Thommes, 2004). Before the analysis, the sample was degassed at 100 °C for 2 h in a nitrogen flow.

As previously described, the hydrophobic-hydrophilic ratio (HI) was performed (Teixeira et al. 2021; Wamba et al. 2017). In addition, the p*H*_{pzc} of the R₁ and R₂ samples were obtained as described elsewhere (Lima et al. 2019b; Teixeira et al. 2021). The elemental analysis (C H N/O) was performed utilizing a Perkin Elmer analyzer (Lima et al. 2019b; Teixeira et al. 2021).

The functional groups of the materials were qualitatively determined using Fourier transform infrared spectroscopy (FTIR) (Bruker Spectrometer) using KBr pellets. The spectrum was recorded with 100 cumulative scans over 4000–400 cm⁻¹ with a resolution of 4 cm⁻¹ (Lima et al. 2019b). In addition, Raman spectra were obtained using a Bruker Bravo spectrometer (Guy et al. 2022).

An adapted Boehm-titration procedure was used to quantify the total amount of acidic and basic groups of the ABC-600 (Goertzen et al. 2010a, b; Oickle et al. 2010a, b).

The thermal stability of the R₁ and R₂ were performed by TGA analysis (TA model SDT Q600) as previously described (Lima et al. 2019b; Thue et al. 2020).

The morphology of composite samples to observe the particle patterns was examined by scanning electron microscopy (SEM) using the Merlin instrument (FESEM, ZEISS Sigma HD) with an in-lens secondary electron detector (dos Reis et al. 2022).

Batch adsorption experiments

An aliquot of 20.00 mL of CIP (see Fig. S1) solution with the initial concentration varying from 5.0 to 200.0 mg L⁻¹ was added to 50.0-mL flat Falcon tubes with 30.0 mg of R₁ and R₂ composite samples at pH ranging 2.0–10.0. The Falcon tubes were capped and disposed of horizontally inside a thermostatic reciprocating agitator (Oxy 350, São Leopoldo, Brazil). The slurries were shaken at different time intervals between 1 and 360 min at 10° to 45 °C with a shaking speed of 120 strikes per minute (Teixeira et al. 2021). Subsequently, the solid phase was separated from the liquid phase by centrifugation. When necessary, aliquots of 1–10 ml of the liquid phase were diluted to 1.0–25.0 mL in calibrated volumetric flasks using the blank solution. Ciprofloxacin unadsorbed after the adsorption process was measured using the T90+ PG Instruments spectrophotometer at a maximum absorption wavelength of 273.0 nm (de Oliveira et al. 2019).

The sorption capacity (Eq. 1) and the percentage of CIP removed (Eq. 2) are given below:

$$q = \frac{(C_0 - C_f)}{m} \cdot V \quad (1)$$

$$\% \text{ Removal} = 100 \cdot \frac{(C_0 - C_f)}{C_0} \quad (2)$$

q is the sorption capacity of CIP adsorbed by the adsorbent (mg g⁻¹). *C*₀ is the initial CIP solution concentration in contact with the solid adsorbent (mg L⁻¹). *C*_{*f*} is the final CIP concentration after adsorption (mg L⁻¹). *m* is the mass of adsorbent (g). *V* is the aliquot of the pharmaceutical solution (L) introduced in the flask.

The study of the influence of the initial pH of CIP was performed at 25 °C, using an initial concentration of 100 mg L⁻¹ of the pharmaceutical solution, a time of contact between the adsorbent and adsorbates of 2 h, an adsorbent dosage of 1.5 g L⁻¹, and pH ranging from 2.0 to 10.0.

The kinetic and equilibrium data's fitness was done using nonlinear methods, which were evaluated using the

Simplex method and the Levenberg–Marquardt algorithm using the fitting facilities of the Microcal Origin 2021 software (Lima et al. 2021a). The suitability of the kinetic and equilibrium models was evaluated using the residual sum of squares (RSS), the determination coefficient (R^2), the adjusted determination coefficient (R^2_{adj}), the standard deviation of residues (SD), and also the Bayesian Information Criterion (BIC) (Lima et al. 2021a, 2021b). Equations 3, 4, 5, 6 and 7 are the mathematical expressions for respective RSS , R^2 , R^2_{adj} , SD , and BIC .

$$RSS = \sum_i^n (q_{i,exp} - q_{i,model})^2 \quad (3)$$

$$R^2 = \left(\frac{\sum_i^n (q_{i,exp} - \bar{q}_{i,exp})^2 - \sum_i^n (q_{i,exp} - q_{i,model})^2}{\sum_i^n (q_{i,exp} - \bar{q}_{i,exp})^2} \right) \quad (4)$$

$$R^2_{adj} = 1 - (1 - R^2) \cdot \left(\frac{n-1}{n-p-1} \right) \quad (5)$$

$$SD = \sqrt{\left(\frac{1}{n-p} \right) \cdot \sum_i^n (q_{i,exp} - q_{i,model})^2} \quad (6)$$

$$BIC = nLn\left(\frac{RSS}{n}\right) + pLn(n) \quad (7)$$

In the above equations, $q_{i,model}$ is the individual theoretical q value predicted by the model; $q_{i,exp}$ is individual experimental q value; \bar{q}_{exp} is the average of all experimental q values measured; n is the number of experiments; and p is the number of parameters in the fitting model.

The values of R^2_{adj} , SD , and BIC will be presented to compare different models of kinetics and equilibrium presented in this work. The best-fitted model would present R^2_{adj} closer to 1.000, lower values of SD , and BIC values. However, the kinetic and equilibrium model could not merely be chosen based on the values of R^2 (Lima et al. 2021a, 2021b) when these models present a different number of parameters. Therefore, it is necessary to check if the R^2 values' improvements are due to the increase of a number of the parameters (Lima et al. 2021a, 2021b) or if, physically, the model with more parameters explains better the process taking place (Lima et al. 2021a, 2021b).

However, the difference in BIC values between models could be conclusive if the difference in BIC values ≤ 2.0 ; there is no significant difference between the two models (Lima et al. 2021a, 2021b). When BIC values' difference is within 2–6, there is a positive perspective that the model with lower BIC is the most suitable (Lima et al. 2021a, 2021b). For variations of BIC values from 6 to 10, there is a strong possibility

that the model with a lower BIC value is the best model to be fitted [43,44]. However, if the difference in BIC values ≥ 10.0 , it can be predicted with accuracy that the model with a lower BIC value is better fitted (Lima et al. 2021a, 2021b).

Kinetics and equilibrium adsorption models

Pseudo-first-order, pseudo-second-order, and Avrami fractional-order (Lima et al. 2021a) models were used to fit the kinetic data. The mathematical equations of these respective models are shown in Eqs. 8, 9, and 10.

$$q_t = q_e \cdot [1 - \exp(-k_1 t)] \quad (8)$$

$$q_t = \frac{k_2 \cdot q_e^2 \cdot t}{1 + q_e \cdot k_2 \cdot t} \quad (9)$$

$$q_t = q_e \cdot [1 - \exp(-k_{AV} \cdot t)^{n_{AV}}] \quad (10)$$

where t is the contact time (min); q_t , q_e are the amount of adsorbate adsorbed at time t and the equilibrium, respectively (mg g^{-1}); k_1 is the pseudo-first-order rate constant (min^{-1}); k_2 is the pseudo-second-order rate constant ($\text{g mg}^{-1} \text{min}^{-1}$); k_{AV} is the Avrami fractional-order constant rate (min^{-1}); and n_{AV} is the Avrami exponent ($n > 0$).

Langmuir, Freundlich, and Liu's models were employed to analyze equilibrium data. Equations 11, 12, and 13 show the corresponding Langmuir, Freundlich, and Liu models (Lima et al. 2021a).

$$q_e = \frac{Q_{max} \cdot K_L \cdot C_e}{1 + K_L \cdot C_e} \quad (11)$$

$$q_e = K_F \cdot C_e^{1/n_F} \quad (12)$$

$$q_e = \frac{Q_{max} \cdot (K_g \cdot C_e)^{n_L}}{1 + (K_g \cdot C_e)^{n_L}} \quad (13)$$

where q_e is the adsorbate amount adsorbed at equilibrium (mg g^{-1}); C_e is the adsorbate concentration at equilibrium (mg L^{-1}); Q_{max} is the maximum sorption capacity of the adsorbent (mg g^{-1}); K_L is the Langmuir equilibrium constant (L mg^{-1}); K_F is the Freundlich equilibrium constant [$\text{mg g}^{-1} \cdot (\text{mg L}^{-1})^{-1/n_F}$]; K_g is the Liu equilibrium constant (L mg^{-1}); and n_F and n_L are the exponents of Freundlich and Liu model, respectively (n_F and n_L are dimensionless).

Adsorption thermodynamics

Thermodynamic studies for the CIP adsorption onto R_1 and R_2 adsorbents were performed at temperatures ranging from 10 to 45 °C (283 to 318 K).

The Gibb’s free energy change (ΔG^0 , kJ mol⁻¹), enthalpy change (ΔH^0 , kJ mol⁻¹), and entropy change (ΔS^0 , J mol⁻¹ K⁻¹) were evaluated with the aid of Eqs. 14, 15, 16 and 17, respectively (Lima et al. 2019a, 2019b, 2020).

$$\Delta G^0 = \Delta G^0 - T.\Delta S^0 \tag{14}$$

$$\Delta G^0 = -RT.LnK_e^0 \tag{15}$$

$$K_e^0 = \frac{(1000.K_g.M_w.[adsorbate]^0)}{\gamma} \tag{16}$$

The combination of Eqs. 14 and 15 leads to Eq. 17

$$LnK_e^0 = \frac{\Delta S^0}{R} - \frac{\Delta H^0}{R}.\frac{1}{T} \tag{17}$$

R is the universal gas constant (8.314 J K⁻¹ mol⁻¹); T is the absolute temperature (Kelvin); M_w is the molecular weight of the adsorbate (g mol⁻¹), $[adsorbate]^0$ is the standard molar concentration of the adsorbate, which by definition is 1 mol L⁻¹; γ is the activity coefficient of the adsorbate. K_e^0 is the thermodynamic equilibrium constant, calculated according to Eq. 16. K_e^0 is dimensionless (Lima et al. 2019a, 2019b).

K_e^0 is calculated by converting K_g values (Liu equilibrium constant) or K_L (Langmuir equilibrium constant), expressed in L mg⁻¹ into L mol⁻¹. Firstly, the value K_g or K_L is multiplied by 1000 (mg g⁻¹) and then multiplied by the molecular

weight of the adsorbate (g mol⁻¹) and by the standard concentration of the adsorbate (1 mol L⁻¹) and divided by the activity coefficient of the adsorbate (γ -dimensionless) (Lima et al. 2019a, 2019b). It is assumed that the solution is sufficiently diluted to consider that the γ is unitary (Lima et al. 2019a, 2019b). Making these calculations, K_e^0 becomes dimensionless (Lima et al. 2019a, 2019b).

Equation 17 is the linearized van’t Hoff equation (Lima et al. 2020). On the other hand, recently, Lima et al. 2020 proposed using the nonlinear van’t Hoff equation, as presented in Eq. 18.

$$K_e = exp\left[\frac{\Delta S}{R} - \left(\frac{\Delta H}{R}\right).\frac{1}{T}\right] \tag{18}$$

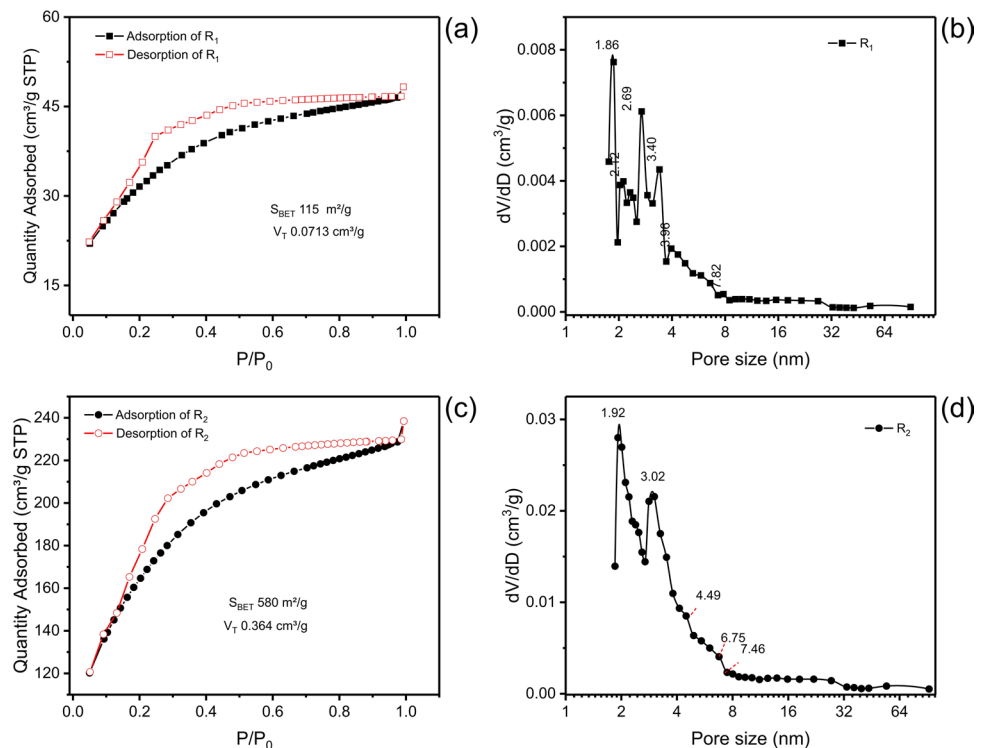
Results and discussion

Textural characteristics

Figure 1 shows the isotherms of adsorption and desorption of N₂ and the pore size distribution curves according to the DFT method for R₁ and R₂ composite samples.

There is a remarkable difference in the textural properties of composite materials. R₁ sample presents a surface area of 115 m² g⁻¹ and a total pore volume of 0.0713 cm³g⁻¹. Conversely, the R₂ sample presents a surface area of 580 m² g⁻¹ and a total pore volume of 0.364 cm³ g⁻¹. It is crucial to focus that although the adsorption isotherm of adsorption

Fig. 1 Textural characteristics of R₁ and R₂ samples. **a** Isotherm of adsorption of R₁; **b** pore size distribution of R₁; **c** isotherm of adsorption of R₂; **d** pore size distribution of R₂



of N_2 seems to be classified as type I (Thommes et al. 2015), they present hysteresis type H2(b) (Thommes et al. 2015). This type of loop hysteresis is associated with a wide size distribution of neck widths of the pores (Thommes et al. 2015). The ratio P/P_0 to about 0.2 is assigned to a monolayer of nitrogen formation over both composite adsorbents (Thommes et al. 2015).

The pore size distribution curves of the materials seem to be a mixture of microporous materials (pore diameter < 2 nm) and mesopores with diameter < 8 nm (Fig. 1B and D).

It is expected that R_2 composite material would present a higher sorption capacity for removal of CIP from waters than R_1 due to the higher surface area and total pore volume (dos Reis et al. 2016; Thue et al. 2020). This enhancement of the expected sorption capacity of R_2 material over R_1 is due to the pore-filling mechanism. Although this mechanism is essential for removing solutes dissolved in water, it is not the unique mechanism that should be considered (Cunha et al. 2020; Thue et al. 2017).

Figure S3 shows the SEM images of R_1 and R_2 composite samples, respectively. There are no remarkable differences between the two composite materials. In the R_1 sample, an irregular material deposit is seen over other materials. This deposit could be chains of MK polysiloxane covering the avocado biochar. In the R_2 composite sample, the layer of MK polysiloxane seems to be shorter than the one covering R_1 . The results of EDS (data not shown) did not reveal remarkable differences in the Si content in both samples; however, further analysis will show that the R_1 material presents more Si content when compared to the R_2 sample.

Qualitative analysis

With the aim of identifying the main functional groups present on the surface of the R_1 and R_2 composite materials, FTIR spectra were recorded, contributing to a better understanding of how the composite materials could interact with the CIP adsorbate (see Fig. 2).

Both composite materials present very similar FTIR spectra. The band at 3417 (R_1) and 3415 cm^{-1} (R_2) corresponds to the stretching of the -OH group (de Oliveira Carvalho et al. 2019; Caicedo et al. 2020). Considering that these bands are broad, they should be overlapping with -NH groups. For R_1 , the bands at 2968 (asymmetric), 2922 (asymmetric), and 2854 cm^{-1} (symmetric) could be assigned to the stretch of C-H groups (Thue et al. 2017; Wamba et al. 2017), and for R_2 , the bands at 2976 (asymmetric), 2920 (asymmetric), and 2856 cm^{-1} (symmetric) are C-H stretching (Thue et al. 2017; Wamba et al. 2017). The bands at 1691 (R_1) and 1689 cm^{-1} (R_2) are assigned to the stretching of the C=O carboxylic acid functional group in biochar (Guy et al. 2022; Teixeira

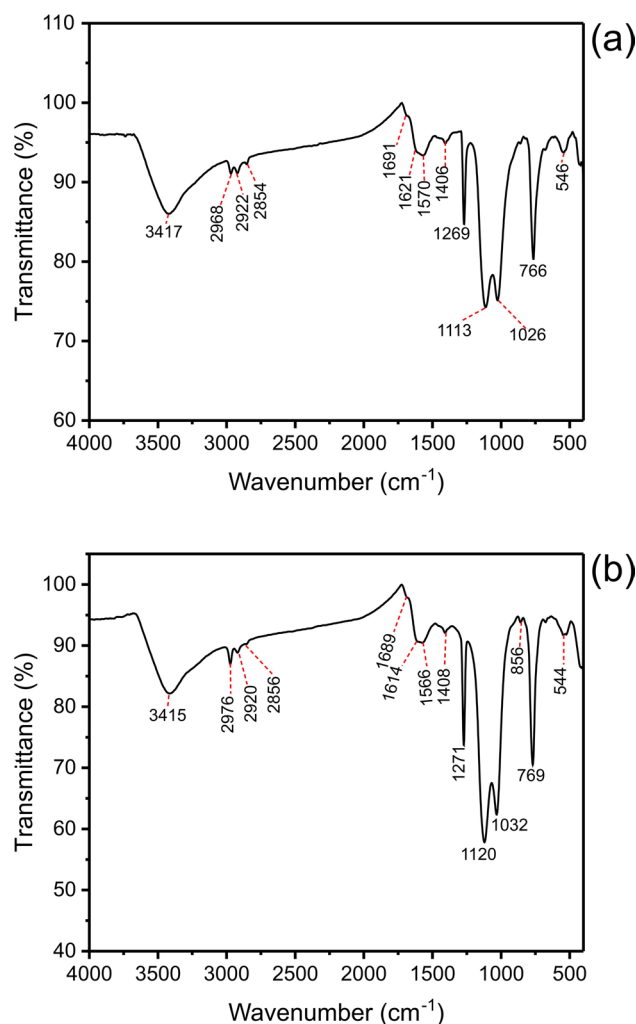


Fig. 2 FTIR spectra: a R_1 and b R_2

et al. 2021). The bands at 1621 and 1570 (R_1) and 1614 and 1566 cm^{-1} (R_2) are attributed to aromatic rings mode (dos Reis et al. 2022; Tomul et al. 2020). A broadening of these bands was observed, that is, characteristics of organo-silicate materials (dos Reis et al. 2016; Teixeira et al. 2021). In addition, the bands at 1570 (R_1) and 1566 cm^{-1} (R_2) can also be attributed to the overlap of NH_2 bending bands with aromatic ring modes (dos Reis et al. 2016; Teixeira et al. 2021). The small bands at 1406 (R_1) and 1408 (R_2) are attributed to aromatic ring modes (Thue et al. 2017; Wamba et al. 2017). The bands at 1269 (R_1) and 1271 cm^{-1} (R_2) are assigned to the C-O stretching of the phenolic group present on the biochar (Lima, DR et al. 2019a; b) or alternatively to Si-CH₃ of MK present in both samples (dos Reis et al. 2016; Teixeira et al. 2021). The bands at 1110 (R_1), and 1120 cm^{-1} (R_2) are assigned to C-O of secondary alcohols present in the biochar. Both composite materials present a band at 1026 (R_1), and 1032 cm^{-1} (R_2) attributed to the Si-O-Si stretch

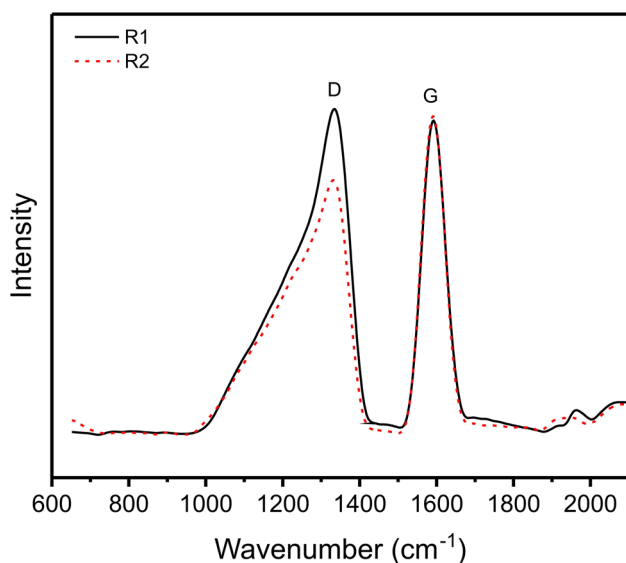


Fig. 3 Raman spectra

of composite material (dos Reis et al. 2016; Teixeira et al. 2021) or primary alcohol C–O groups stretch (Cunha et al. 2020; Thue et al. 2017). The band at 766 (R_1) and 769 cm^{-1} (R_2) are attributed to Si–O stretching (Çok and Gizli 2020; Thue et al. 2017).

The Raman spectra of R_1 and R_2 composites are depicted in Fig. 3.

Raman spectroscopy was carried out to deeply explore the structure and degree of graphitization of the R_1 and R_2 composite materials. Two distinct Raman shifts are observed in the spectra. The first one (D-band), centered at 1332 cm^{-1} , is assigned to sp^3 electronic states (considered defects in the planar sp^2 graphitic structure) corresponding to graphite's low symmetry carbon structure (dos Reis et al. 2022). The second band (G-band), centered at 1592 cm^{-1} , reflects the structural integrity of sp^2 -hybridized carbon atoms (dos Reis et al. 2022). These two types of carbon are present in the BCs phase.

The qualities of the samples were evaluated by comparing the D to G band intensity (the ID/IG ratio). The ID/IG ratio is often below a couple of percent for high-quality samples with higher graphitization. Therefore, higher ID/IG ratio values mean carbon structure with several defects, and low values mean carbon samples with a higher organization (dos Reis et al. 2022). The value of ID/IG for R_1 was 1.04, and for R_2 , it was 0.800. These results show that the grafting of MK polysiloxane onto avocado biochar led to a more organized R_2 composite sample when less MK is grafted in the biochar (data will be shown in the next section that R_2 presents less Si than the R_1 sample).

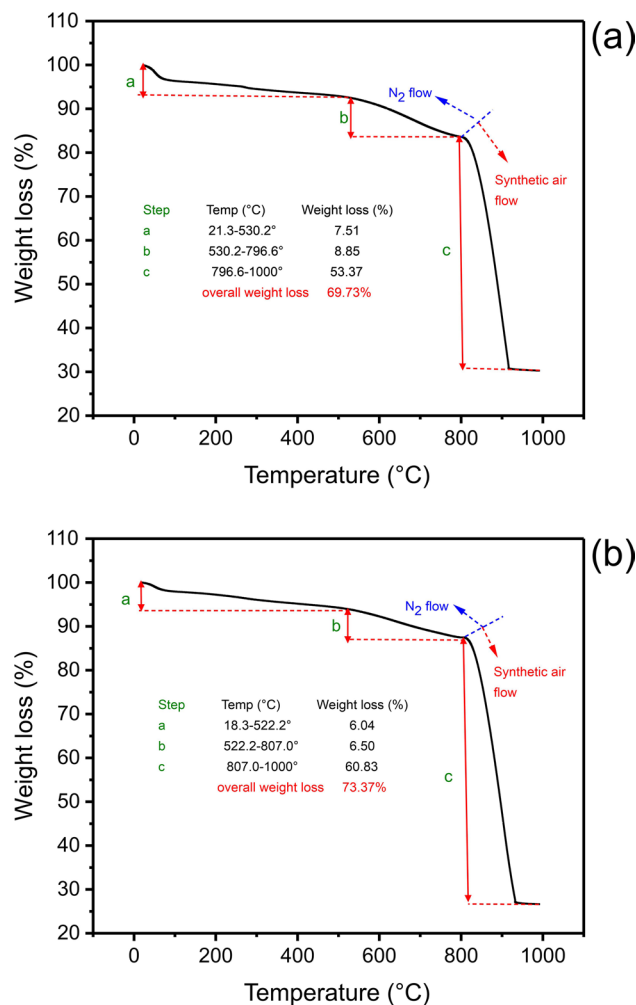


Fig. 4 TGA analysis: **a** R_1 and **b** R_2 . From room temperature up to 800 °C, the gas utilized was N_2 . From 800 to 1000 °C, the gas utilized was synthetic air

Quantitative analysis

The thermal gravimetric analyses of R_1 and R_2 composite samples are shown in Fig. 4. The thermal behavior of both composite samples is similar, presenting three main weight losses. This analysis utilized nitrogen from room temperature up to 800 °C and then from 800 to 1000 °C; the atmosphere was changed from inert to oxidizing utilizing synthetic air (Cunha et al. 2020; Lima et al. 2019a; b; Teixeira et al. 2021; Thue et al. 2020).

In the first stage, 21.3–530.2 °C (R_1) and 18.3–522.2 °C (R_2) comprise the water losses associated with some small decomposition of volatile organics present in the avocado biochar (Cunha et al. 2020; Leite et al. 2018; Lima et al. 2019b; Teixeira et al. 2021) or the loss of methyl group present in the MK siloxane (dos Reis et al. 2016). However, these weight losses were only 7.51% (R_1) and 6.04% (R_2), showing the high-thermal stability of both composite samples. The second

stage was 530.2–796.6 °C (R_1) and 522.2–807.0 °C (R_2), which could be assigned to some degradation of carbon material of biochar. Again, this weight loss was not remarkable for both samples (8.85% R_1 and 6.50% R_2), which indicates that from room temperature up to close to 800 °C, the total weight loss under nitrogen stream was 16.36% (R_1) and 12.54% (R_2). These values indicate that both composite materials present very high thermal stability.

In the third stage, under a synthetic air atmosphere, the weight losses were remarkably increased to 53.37% (R_1) and 60.83% (R_2). This third weight loss corresponds to the total degradation of the composite materials' carbonaceous matrix, leading to a total weight loss including the three stages up to 69.73% (R_1) and 73.37% (R_2). Therefore, the residual mass left in the crucible was 30.27% (R_1), and 26.63% (R_2) could be assigned to the ashes of the composite samples since the third stage was conducted under a synthetic air atmosphere (Cunha et al. 2020; Lima et al. 2019a; b; Teixeira et al. 2021; Thue et al. 2020).

Based on these residue's contents, it is possible to infer that the contents of MK incorporated in R_1 were higher than in the R_2 sample. This result is consistent with the time of exposition of avocado biochar with MK polysiloxane. In the R_1 sample, the avocado biochar was added immediately after the dissolution of MK in ethanol, and they remained together for 48 h of contact. On the other hand, for the R_2 sample, the avocado biochar was added after 48 h of dissolution of MK polysiloxane in ethanol, allowing to form oligomers of MK in ethanol, adding the avocado biochar, and keeping it together for just one hour of contact.

The C H N elemental analysis is depicted in Table 1. The contents of carbon present in R_1 are compatible with a higher composite formation between avocado biochar and MK polysiloxane because then its value is lower (53.64% C) when compared with the R_2 sample (61.22% C), and also the value is also compatible with the contents of ashes determined by TGA analysis, described previously. The contents of H and N were also determined by CHN elemental analysis, and the values are depicted in Table 1. The atomic ratio C/H is 1.20 (R_1) and 1.71 (R_2). How much the C/H atomic ratio is closer to 2, the higher the degree of aromaticity. Conversely, when the atomic ratio of C/H is closer to 1, higher is the aliphatic portion (dos Reis et al. 2022).

This behavior could be easily explained by imaging the condensation of several aromatic rings. For each aromatic ring (C_6H_6), when they are fused, it is necessary

to lose two atoms of hydrogen, forming $C_{10}H_8$ for two rings, $C_{14}H_{10}$ for three fused aromatic rings, $C_{18}H_{14}$ for four fused aromatic rings, $C_{22}H_{18}$ for five fused rings, and $C_{26}H_{22}$ for six fused aromatic rings. Therefore, for each fusion of two aromatic rings, the number of carbon increases by four, and the number of hydrogen increases by two (ratio of 2C for 1H).

Considering that the methyl group number of MK polysiloxane is higher when more of this MK is grafted on the biochar. Therefore, the values of C H N elemental analysis are compatible with a higher amount of MK grafted on R_1 when compared with the R_2 sample.

The total acidity and basicity of the composite samples were quantified using the Bohem titration (Goertzen et al. 2010a, b; Oickle et al. 2010a, b), and the contents of these groups are depicted in Table 1. The higher the sum of acidic plus basic groups, the more polar the surface of the adsorbent.

The HI ratio is given by the equation below (dos Reis et al. 2016; Cunha et al. 2020):

$$HI = \frac{\text{amount of n-heptane vapor (mg)} / \text{adsorbent mass (g)}}{\text{amount of water vapor (mg)} / \text{adsorbent mass (g)}} \quad (19)$$

The HI values of R_1 and R_2 samples are also depicted in Table 1. The values of HI were 1.725 (R_1) and 1.051 (R_2). According to Eq. 19 given above, the higher values of HI mean a higher tendency of the adsorbent surface to uptake hydrophobic molecules. As discussed previously, the sum of acidic plus basic groups was 0.2081 mmol g^{-1} (R_1) and 0.5742 (R_2). Comparing the values of HI with the sum of polar groups (acidic plus basic groups), it can be observed that a higher amount of polar groups leads to a low value of HI, as previously observed in several cases already reported in the literature (Cunha et al. 2020; dos Reis et al. 2016; Lima et al. 2019a; b; Leite et al. 2017; Teixeira et al. 2021; Thue et al. 2020). Another important correlation is that the higher the amount of MK incorporated, the higher the hydrophobicity and HI value. Considering that the R_1 sample presented a higher amount of MK grafted on the biochar, this material presents a higher HI value.

The values of pH_{pzc} of R_1 and R_2 were 5.09 and 4.91, respectively (Table 1), showing no remarkable difference in the acidity behavior of these two composite materials.

Table 1 CHN/O elemental analysis, HI, total acidity and total basicity, and pH_{pzc} for R_1 and R_2 composites

	C (%)	H (%)	N (%)	O (%)	Ashes (%)	Total acidity (mmol g^{-1})	Total basicity (mmol g^{-1})	HI	pH_{pzc}
R_1	53.64	3.76	1.05	11.28	30.27	0.1025	0.1056	1.725	5.09
R_2	61.22	3.01	1.14	8.00	26.63	0.2617	0.3125	1.051	4.91

Table 2 Kinetic parameters for adsorption of CIP onto R₁ and R₂ composite adsorbents. Conditions: C₀ = 100 mg L⁻¹; T = 25 °C, the adsorbent dosage = 1.5 g L⁻¹, pH = 7. All values are expressed with four significant digits

	R ₁	R ₂
Pseudo-first order		
q _e (mg g ⁻¹)	6.208	41.41
k ₁ (min ⁻¹)	0.03993	0.05762
t _{1/2} (min)	17.36	12.03
t _{0.95} (min)	75.02	52.00
R ² adjusted	0.9133	0.9536
SD (mg g ⁻¹)	0.6522	3.231
BIC	-12.34	61.27
Pseudo-second order		
q _e (mg g ⁻¹)	6.812	45.11
k ₂ (g mg ⁻¹ min ⁻¹)	0.008730	0.001759
t _{1/2} (min)	15.38	11.78
t _{0.95} (min)	165.2	140.9
R ² adjusted	0.9670	0.9905
SD (mg g ⁻¹)	0.4025	1.459
BIC	-34.54	24.70
Avrami fractional-order		
q _e (mg g ⁻¹)	7.677	44.87
K _{AV} (min ⁻¹)	0.01672	0.03720
n _{AV}	0.4750	0.5851
t _{1/2} (min)	20.52	14.00
t _{0.95} (min)	246.4	157.6
R ² adjusted	0.9999	0.9975
SD (mg g ⁻¹)	0.02070	0.7514
BIC	-169.1	-3.818

Effect of pH

The influence of the adsorbate solution's initial pH on the sorption capacity is one of the main variables that could affect the uptake of a molecule in an adsorbent (Kudo et al. 2020; Tomul et al. 2020).

The value of pH_{pzc} also influences the sorption capacity of the adsorbent. For pH values > pH_{pzc}, the adsorbent surface becomes negatively charged, and for pH values < pH_{pzc}, the adsorbent surface becomes positively charged (Leite et al. 2017; Lima et al. 2019a). Also, the pK_a values of the adsorbate influence the sorption capacity of an adsorbent. Figure S4 shows the CIP species at pH ranging from 0 to 14 (de Oliveira Carvalho et al. 2019). The pK_a values of CIP are pK_{a1} 5.56 and pK_{a2} 8.77. Therefore, CIP has three species with different proportions depending on the pH value (see Fig. S4). At pH 7.0, species 1 contributes 3.48%, species 2 contributes 94.84%, and species 3 contributes 1.63% of all the species (de Oliveira Carvalho et al. 2019). Then, the zwitterionic species is predominant at pH 7 (species 2; see Fig. S4). Assays of the effect of initial CIP pH ranging

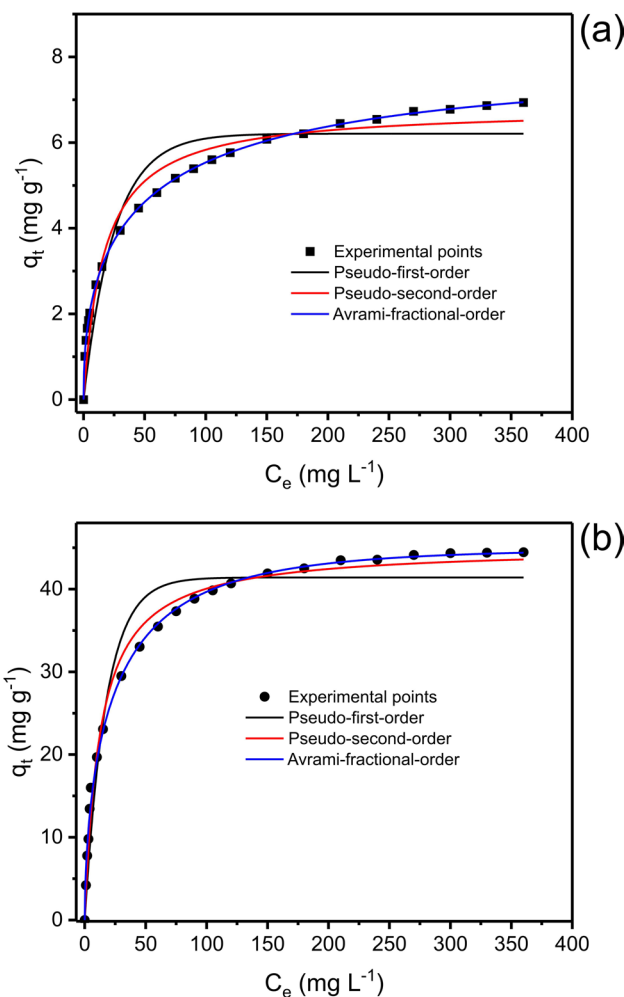


Fig. 5 Kinetic Curves for CIP adsorption onto **a** R₁ and **b** R₂ composite adsorbents. Conditions: the initial CIP concentration was 100 mg L⁻¹, the temperature was fixed at 25 °C, the adsorbent dosage of 1.5 g L⁻¹, and initial pH of the adsorbate solution was 7.0

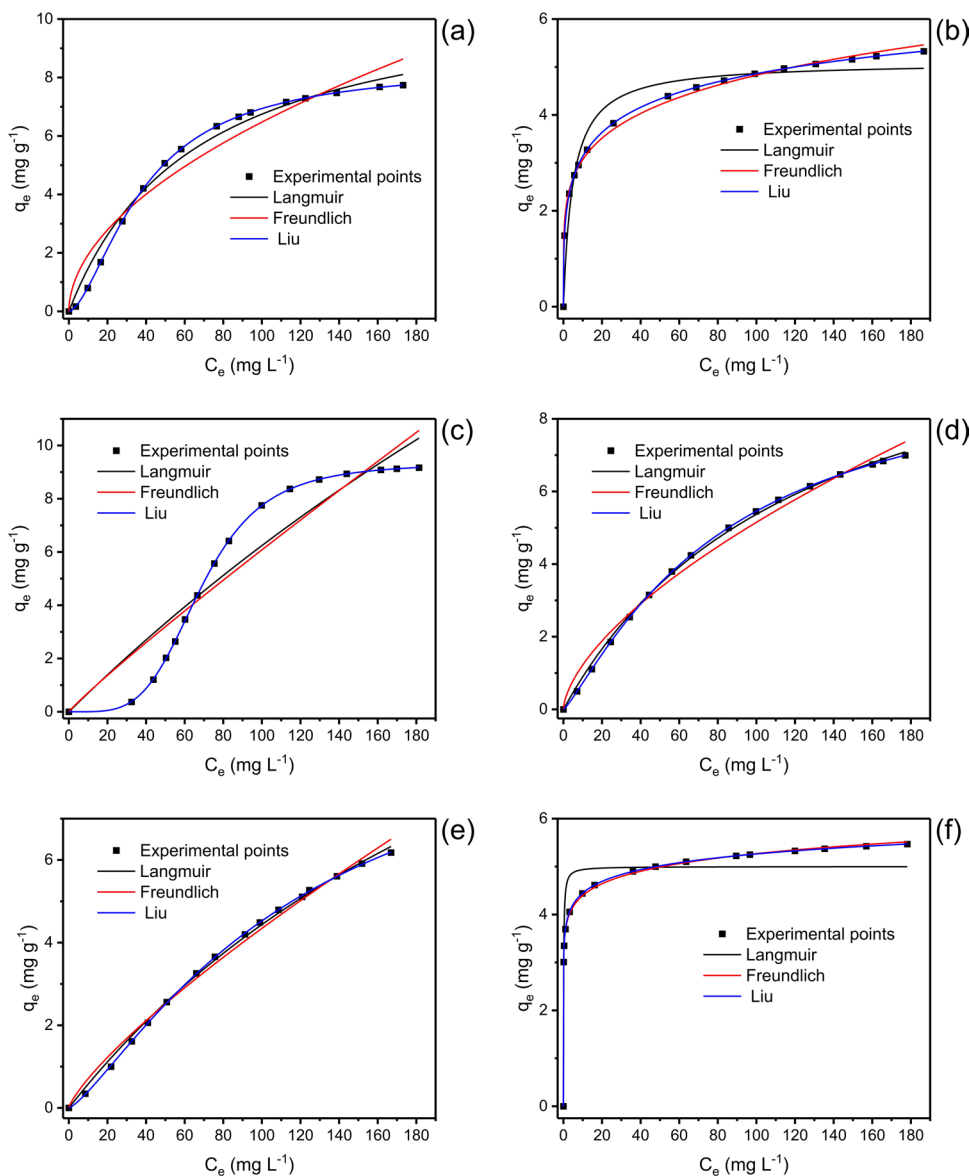
from 3.5 to 12 demonstrated that the removal percentage of CIP did not suffer a remarkable variation (changes < 2.3%). Then, in the next adsorption experiments, the pH of the adsorbate solution was fixed at 7.0 to continue this research.

It is important to highlight that at pH 7.0, the surface of R₁ and R₂ samples will be negatively charged; however, the predominant species of CIP is a zwitterionic species (94.84%) (de Oliveira Carvalho et al. 2019); therefore, electrostatic attraction of the quaternary ammonium salt with the negatively charged adsorbent could take place.

Kinetic studies

The kinetics adsorption data of the CIP antibiotic onto R₁ and R₂ composite samples were carried out utilizing the pseudo-first-order, pseudo-second-order, and Avrami fractional-order (Lima et al. 2021a; b), and the parameters of the

Fig. 6 Isotherms of adsorption of CIP on R1 adsorbent. **a** 10 °C; **b** 20 °C; **c** 25 °C; **d** 30 °C; **e** 40 °C; **f** 45 °C. Conditions: time of contact 300 min between CIP and R₁; adsorbent dosage 1.5 g.L⁻¹; initial pH 7.0



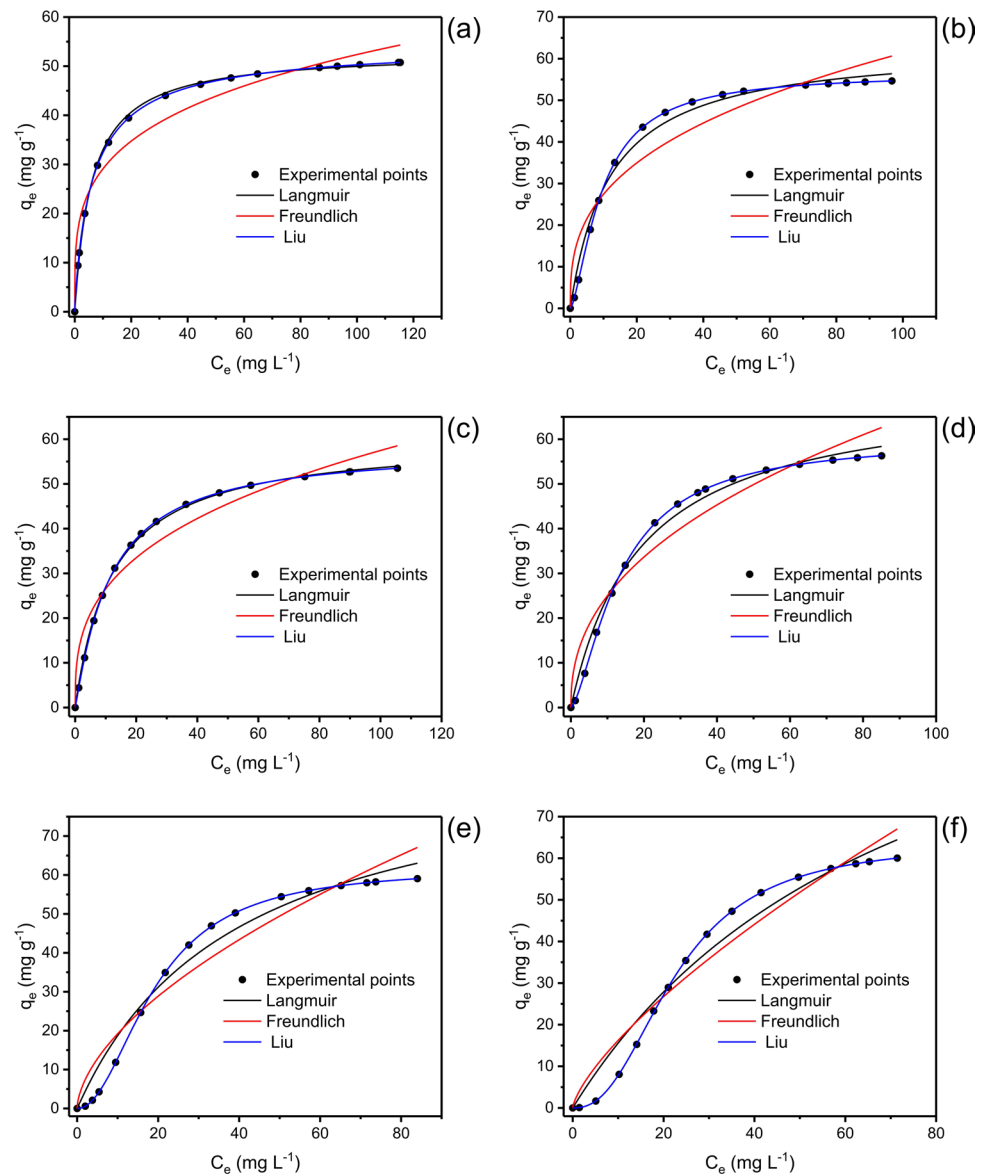
fitted models are shown in Table 2, and the kinetic curves are shown in Fig. 5.

Observing Fig. 5, it is possible to verify that PFO and PSO kinetic adsorption models were not accurately fitted since most experimental points are out of the model curve. On the other hand, a sound analysis of Table 2 clarifies it. The values of R^2_{adj} , SD, and BIC show that the Avrami fractional-order kinetic adsorption model was the unique model that described the kinetic adsorption data well because the values of R^2_{adj} are closer to 1.00 and the values of SD and BIC were lower than compared with PFO and PSO. As reported earlier (Lima et al. 2021a; b), the Bayesian information criterion (BIC) is a statistical analysis that establishes the best-fitted model because when ΔBIC (BIC model 1 – BIC model 2) < 2, there is no remarkable difference

between the two models, and when $\Delta BIC > 10$, certainly the model with lower BIC value is the model that better describes the physical phenomenon (Lima et al. 2021a; b). The ΔBIC between PFO and Avrami and PSO and Avrami were, respectively, 156.7 and 134.5 for R₁ adsorbent and 65.09 and 28.52 for R₂ adsorbent. Therefore, the statistical analysis confirms that the Avrami fractional kinetic model describes the adsorption kinetics for CIP uptake using R₁ and R₂ adsorbents.

Considering that it is not easy to compare different kinetic models because the constant rates present different units (see Table 2), the values of $t_{1/2}$ and $t_{0.95}$ were obtained by interpolation in the fitted curve for the time necessary to attain 50% and 95% of the saturation, respectively (Lima et al. 2019b; Teixeira et al. 2021; Wamba et al. 2017). These

Fig. 7 Isotherms of adsorption of CIP on R₂ adsorbent. **a** 10 °C; **b** 20 °C; **c** 25 °C; **d** 30 °C; **e** 40 °C; **f** 45 °C. Conditions: time of contact 180 min between CIP and R₂; adsorbent dosage 1.5 g·L⁻¹; initial pH 7.0



time parameters mean the time necessary to attain 50% and 95% of the saturation, respectively. Considering that the Avrami fractional-order kinetic model was the best-fitted model, it can be assumed that the times to attain 95% of saturation were 246.4 min (R₁) and 157.6 min (R₂). Based on this result, it was established that the equilibrium studies should employ a contact time between the adsorbent and the adsorbate of 300 min (R₁) and 180 min (R₂) for performing these experiments.

This difference in the contact time to attain the equilibrium is coherent with the total pore volume of R₁ (0.0713 cm³ g⁻¹) and R₂ (0.364 cm³ g⁻¹) composite materials, as earlier reported for other adsorbents (Cunha et al. 2020; Lima et al. 2019a). Therefore, higher total pore volume will lead to faster kinetics (Cunha et al. 2020; Lima et al. 2019a).

Equilibrium and thermodynamic studies and adsorption mechanism

The equilibrium adsorption studies of CIP onto R1 and R2 composite samples were performed from 10 to 45 °C. The Langmuir, Freundlich, and Liu equilibrium models accessed CIP uptake. The results are depicted in Fig. 6 (R₁) and Fig. 7 (R₂), and the values of equilibrium parameters are shown in Table 3.

Results depicted in Table 3 show that the Liu equilibrium model was the best equilibrium model for all the studied temperatures (10 to 45 °C) due to R_{adj}^2 being closer to 1 and the lowest BIC and SD values. The ΔBIC between Langmuir and Liu ranged from 50.00 to 220.4 (10–45 °C) using R₁ adsorbent and 72.46 to 206.9 (10–45 °C) using R₂ adsorbent (Lima et al. 2021a; b). The ΔBIC between Freundlich

Table 3 Langmuir, Freundlich, and Liu isotherm parameters for CIP adsorption on R₁ and R₂ adsorbents. Adsorbent dosage = 1.5 g L⁻¹, pH = 7.0. Time of contact between CIP and adsorbent, 300 min R₁, 180 min R₂. All values are expressed with four significant digits

	10 °C	20 °C	25 °C	30 °C	40 °C	45 °C
R₁						
Langmuir						
Q_{max} (mg g ⁻¹)	11.18	5.102	49.95	12.12	17.41	5.001
K_L (L mg ⁻¹)	0.01522	0.2043	0.001427	0.007966	0.003419	7.631
R^2_{adj}	0.9861	0.9446	0.8904	0.9986	0.9975	0.8964
SD (mg g ⁻¹)	0.3330	0.3653	1.135	0.08957	0.1019	0.4518
BIC	-29.00	-26.05	10.24	-71.03	-66.90	-19.27
Freundlich						
K_F (mg.g ⁻¹ .(mg.L ⁻¹) ^{-1/nF})	0.5800	1.947	0.08481	0.2894	0.1156	3.666
n_F	1.909	5.070	1.078	1.600	1.270	12.69
R^2_{adj}	0.9441	0.9955	0.8815	0.9855	0.9916	0.9992
SD (mg g ⁻¹)	0.6682	0.1037	1.180	0.2868	0.1856	0.03861
BIC	-6.721	-66.33	11.48	-33.78	-47.72	-97.95
Liu						
Q_{max} (mg g ⁻¹)	8.411	8.850	9.326	9.838	10.21	10.77
K_g (L mg ⁻¹)	0.02589	0.01768	0.01459	0.01203	0.008371	0.007120
n_L	1.630	0.3473	4.205	1.193	1.288	0.1331
R^2_{adj}	0.9999	0.9999	0.9999	0.9999	0.9999	0.9999
SD (mg g ⁻¹)	0.009476	0.003567	0.01933	0.004233	0.02030	4.384.10 ⁻⁴
BIC	-141.3	-172.6	-118.5	-167.1	-116.9	-239.7
R₂						
Langmuir						
Q_{max} (mg g ⁻¹)	53.00	63.35	60.27	71.40	92.66	131.7
K_L (L mg ⁻¹)	0.1641	0.08369	0.08102	0.05270	0.02532	0.01340
R^2_{adj}	0.9989	0.9893	0.9993	0.9898	0.9712	0.9656
SD (mg g ⁻¹)	0.5614	2.094	0.4748	2.058	4.033	4.284
BIC	-12.30	29.83	-17.66	29.28	50.81	52.74
Freundlich						
K_F (mg.g ⁻¹ .(mg.L ⁻¹) ^{-1/nF})	16.17	12.27	12.26	9.314	4.958	3.080
n_F	3.920	2.861	2.980	2.332	1.701	1.386
R^2_{adj}	0.9453	0.9109	0.9416	0.9333	0.9286	0.9438
SD (mg g ⁻¹)	3.991	6.032	4.361	5.265	6.348	5.479
BIC	50.47	63.99	53.31	59.34	65.32	60.61
Liu						
Q_{max} (mg g ⁻¹)	54.69	56.45	58.18	60.01	61.85	63.80
K_g (L mg ⁻¹)	0.1517	0.1045	0.08729	0.07353	0.05227	0.04414
n_L	0.8947	1.478	1.098	1.486	2.061	2.411
R^2_{adj}	0.9999	0.9999	0.9999	0.9999	0.9999	0.9999
SD (mg g ⁻¹)	0.003858	0.003098	0.04694	0.1754	0.05048	0.1115
BIC	-170.1	-177.1	-90.12	-47.94	-87.79	-62.42

and Liu ranged from 69.18 to 141.8 for R₁ adsorbent and ranged from 107.3 to 241.1 for R₂ adsorbent. Therefore, Δ BIC values were much higher than 10, which allow one to state that the Liu isotherm model was the equilibrium model that could explain the equilibrium data for CIP adsorption onto R₁ and R₂ composite samples at the temperature of 10–45 °C. These results are corroborated with the values of R^2_{adj} closer to 1.00, besides the lowest values of SD (see Table 3).

Taking into account the values of Q_{max} obtained by the Liu isotherm model for R₁ and R₂ samples, it is observed that R₂ presented Q_{max} values 5.92–6.50 times higher than R₁. This remarkable difference is compatible with the differences in the surface area (580 m² g⁻¹ for R₂ versus 115 m² g⁻¹ for R₁) and total pore volume (0.364 cm³ g⁻¹ for R₂ versus 0.0713 cm³ g⁻¹ for R₁). In this sense, pore-filling is one of the main mechanisms of adsorption.

Table 4 Adsorbents utilized for removal of CIP

Adsorbent	Q _{max} (mg g ⁻¹)	Ref
Aluminum dispersed bamboo activated carbon	13.36	Guellati et al. 2022
Chitosan–gelatin-graphene oxide aerogels	8.4	Kovtun et al. 2020
Zinc oxide impregnated activated carbon	15.75	Magesh et al. 2022
Carbon dioxide activated biochar-clay mineral composite	50.32	Arif et al. 2022
Jerivá activated carbon	198.6–335.8	de Oliveira Carvalho et al. 2019
Demolition wastes modified with APTES	98.9–138.0	Caicedo et al. 2020
A polymer composite of magnetic/β-cyclodextrin/activated charcoal/Na alginate	3.125	Yadav et al. 2021
Graphene oxide decorated with halloysite nanotubes (HNTs/GO) composite	467.3–943.4	Wang et al. 2021a
Biochar–clay hybrid adsorbent	140.3	Lawal et al. 2019
Ethylenediaminetetraacetic acid/β-cyclodextrin composite	448	Yu et al. 2018
Metal–organic–framework	1826	Khan et al. 2020
γ-Al ₂ O ₃ nanoparticles	5.12	Najafpoor et al. 2019
Graphene-boron nitride composite aerogel	185	Han et al. 2022
Copper-based metal–organic framework	538	Wu et al. 2018
Magnesium silicate-based sulfonated polystyrene sphere composites	329.7	Wang et al. 2020;
Magnetic nickel cobalt sulfide/sodium dodecyl benzene sulfonate	625	Wu et al. 2021
NiFe ₂ O ₄ @carbon composites	737.42	Lam et al. 2021
Polyamidoamine-functionalized graphene oxide – SBA-15	24.6	Xikhongelo et al. 2021
Hybrid hydrogen-bonded covalent organic polymers	84.03	Yang et al. 2020
Zn(II)-impregnated chitosan/graphene oxide	211.5–227.6	Rahman and Varshney 2021
Biocomposite of regenerated-reed plus reed-charcoal	31.8	Karoui et al. 2020
R ₁	8.41–10.77	This work
R ₂	54.69–63.80	This work

The sorption capacity of R₁ and R₂ were compared with several other adsorbents, as depicted in Table 4 (Arif et al. 2022; Caicedo et al. 2020; de Oliveira et al. 2019; Guellati et al. 2022; Han et al. 2022; Karoui et al. 2020; Khan et al. 2020; Kovtun et al. 2020; Lam et al. 2021; Lawal et al. 2019; Magesh et al. 2022; Najafpoor et al. 2019; Rahman

and Varshney 2021; Wang et al. 2020; Wang et al. 2021a; Wu et al. 2018; Wu et al. 2021; Xikhongelo et al. 2021; Yadav et al. 2021; Yang et al. 2020; Yu et al. 2018).

Out of twenty-three adsorbents, the R₂ composite adsorbent presents a higher sorption capacity of nine (Arif et al. 2022; Caicedo et al. 2020; de Oliveira et al. 2019; Guellati

Table 5 Thermodynamic parameters of the adsorption of CIP on R₁ and R₂ adsorbents. All values are expressed with four significant digits

Temperature (K)	283	293	298	303	313	318
Liu model						
R₁						
K _e ⁰	8.578.10 ³	5.857.10 ³	4.835.10 ³	3.985.10 ³	2.774.10 ³	2.359.10 ³
ΔG ⁰ (kJ mol ⁻¹)	-21.31	-21.13	-21.02	-20.88	-20.63	-20.53
ΔH ⁰ (kJ mol ⁻¹)	-	-	-27.42	-	-	-
ΔS ⁰ (J K ⁻¹ mol ⁻¹)	-	-	-21.54	-	-	-
R ²	-	-	0.9996	-	-	-
R ² _{adj}	-	-	0.9995	-	-	-
Liu model						
R₂						
K _e ⁰	5.026.10 ⁴	3.463.10 ⁴	2.892.10 ⁴	2.436.10 ⁴	1.732.10 ⁴	1.462.10 ⁴
ΔG ⁰ (kJ mol ⁻¹)	-25.47	-25.46	-25.45	-25.45	-25.40	-25.36
ΔH ⁰ (kJ mol ⁻¹)	-	-	-26.10	-	-	-
ΔS ⁰ (J K ⁻¹ mol ⁻¹)	-	-	-2.195	-	-	-
R ²	-	-	0.9999	-	-	-
R ² _{adj}	-	-	0.9998	-	-	-

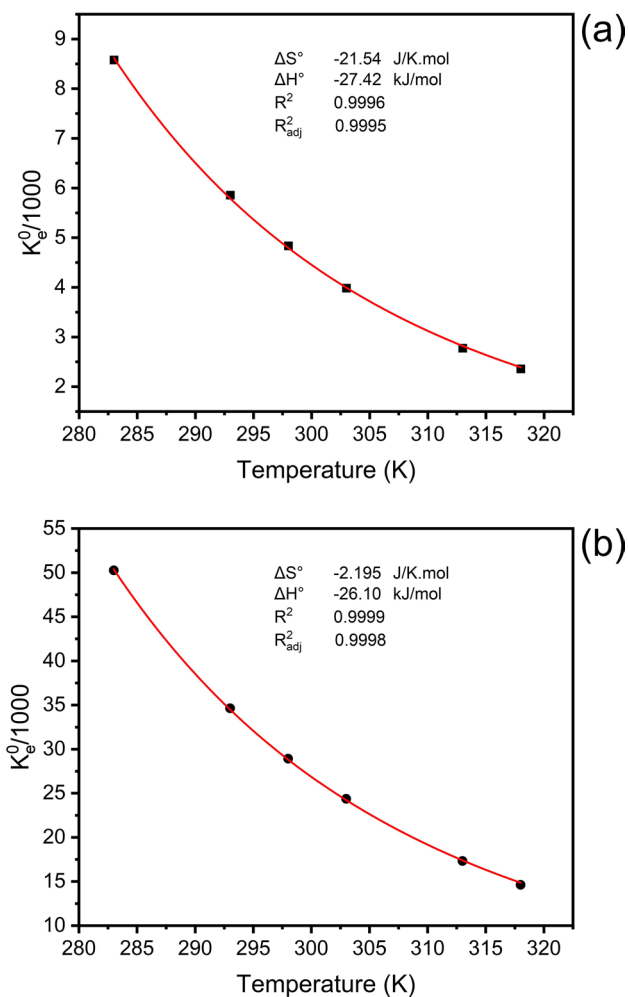
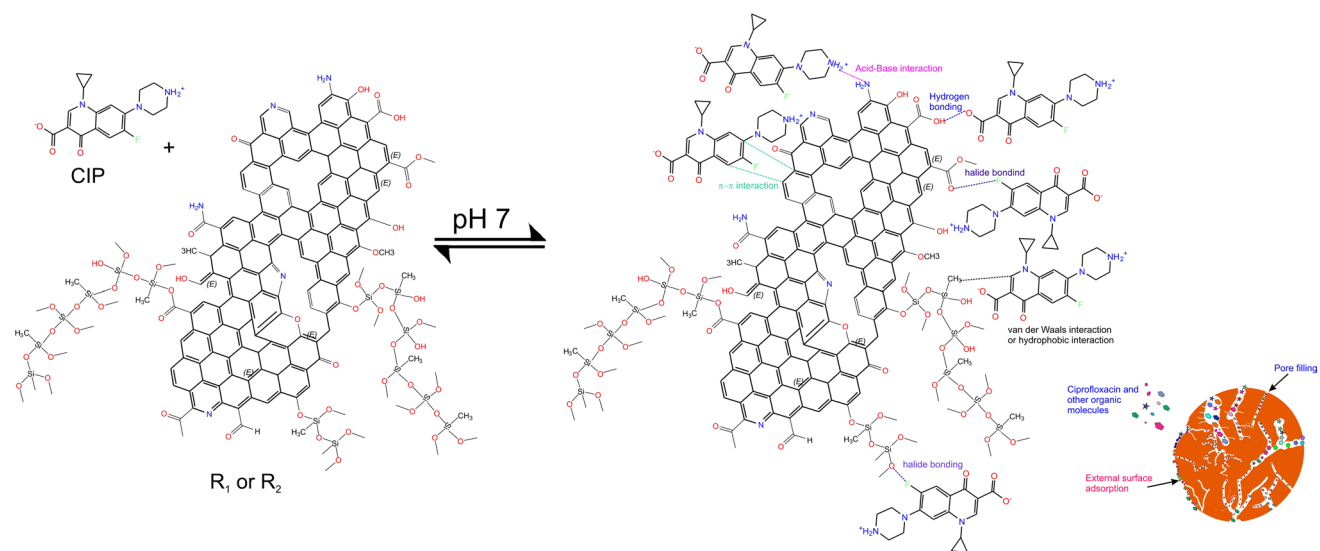


Fig. 8 Nonlinear van't Hoff equation for ciprofloxacin uptake by **a** R_1 and **b** R_2 adsorbents



et al. 2022; Han et al. 2022; Karoui et al. 2020; Khan et al. 2020; Kovtun et al. 2020; Lam et al. 2021; Lawal et al. 2019; Magesh et al. 2022; Najafpoor et al. 2019; Rahman and Varshney 2021; Wang et al. 2020; Wang et al. 2021a; Wu et al. 2018; 2021; Xikhongelo et al. 2021; Yadav et al. 2021; Yang et al. 2020; Yu et al. 2018). The sorption capacity of R_2 material is not remarkable compared to the literature, but it opens possibilities of being improved when other polysiloxanes are employed instead of MK.

Table 5 shows the thermodynamic parameters obtained from the equilibrium data from 10 to 45 °C (283–318 K) using the best-fitted isotherm (Lima et al. 2019a; b) for the uptake of CIP using R_1 and R_2 composite adsorbents. In addition, the nonlinear van't Hoff equation (Lima et al. 2020) is presented in Fig. 8 as depicted in Table 5; all values of ΔG° were negative, indicating that the adsorption process was favorable at the 283–318 K interval.

Observing Fig. 8, the enthalpy variation was negative (exothermic process) for CIP uptake on both composite samples, and the variation of entropy was also negative. These results show that CIP after the adsorption should be in a more organized state than free in the aqueous solution before the adsorption takes place (Lima et al. 2021a). Also, considering the magnitude of enthalpy, the values obtained for both adsorbents are compatible with a physical interaction of the CIP with R_1 and R_2 composite samples (Leite et al. 2017; 2018; Lima et al. 2021a). The adsorption process is controlled by enthalpy because the process is exothermic, which contributes to ΔG° being negative in all the temperature range (283–318 K).

Based on the results of the characterization of the R_1 and R_2 adsorbents, the adsorption studies (adsorption kinetics,

equilibrium, and thermodynamics), it is possible to establish a mechanism of adsorption that is depicted in Fig. 9.

CIP at pH 7.0 is present in the zwitterionic form (see Fig. S4). When this antibiotic is placed with the composite materials R_1 or R_2 , the cationic ammonium group of CIP has an acid–base interaction with donor groups present on the biochar part of the composite material (Tomul et al. 2020). In addition, the anionic group of CIP interacts with OH groups present on the biochar, forming hydrogen bonding (Leite et al. 2017; Tomul et al. 2020). Also, CIP presents a fluoride group that could form halogen bonding with the biochar or with the silane group on R_1 and R_2 (Desiraju et al. 2013). CIP also could form π - π interactions with the aromatic rings present on the biochar part of the composite samples (Leite et al. 2017; Tomul et al. 2020). Besides the polar interactions, CIP could also interact with hydrophobic interactions (van der Waals forces) with the silane group present on the composite samples (Teixeira et al. 2021; Tomul et al. 2020; Wamba et al. 2017). As a result, the silane groups increase the R_1 composite sample's hydrophobicity compared with the R_2 composite sample.

On the other hand, higher coverage of the biochar with silane groups would impair the polar interactions of CIP with the polar groups present on the biochar. Therefore, this statement is justified that the R_1 composite sample presents more Si contents than the R_2 sample (see Fig. 4). Moreover, a pore-filling mechanism explains the CIP uptake by the composite samples, being the composite material with higher surface area and higher total pore volume (R_2) the sample that presented higher sorption capacity to CIP antibiotic.

Conclusion

Two composite materials were prepared by mixing MK polysiloxane with avocado biochar. The synthesis route of both materials is practically the same, only changing the time for the addition of the avocado biochar to the dissolved MK solution in ethanol. The first composite material (R_1), the addition of avocado biochar, was immediately after dissolving the MK in ethanol at reflux. The second composite material (R_2), the addition of avocado biochar, was after 48 h dissolution of MK polysiloxane in ethanol, continuing the reflux for 1 h. The characterization of the R_1 and R_2 composite samples was carried out by isotherms of adsorption and desorption of nitrogen, which show that the surface area and total pore volume of R_2 were more than 5 times higher than R_1 .

Furthermore, results of TGA analysis revealed that the amount of Si contents present on R_1 was higher than R_2 , which provoked a higher hydrophobicity of R_1 (HI 1.725) than R_2 (1.051). In addition, the R_2 composite presented

a higher number of functional groups (acidic plus basic groups) than R_1 . The kinetic experiments of adsorption show that the CIP uptake was faster in R_2 ($t_{1/2}$ 14.00, $t_{0.95}$ 157.6 min) when compared to R_1 composite sample ($t_{1/2}$ 20.52, $t_{0.95}$ 264.4 min). This faster kinetics is due to the higher pore volume of R_2 material. The equilibrium studies of R_1 and R_2 composite samples were obtained from 10 to 45 °C (283–318 K) using three isotherm models. The best-fitted equilibrium results were obtained using the Liu isotherm model. The thermodynamic studies indicated that the adsorption process was favorable, spontaneous, and exothermic, and the magnitude of enthalpy changes was consistent with physical adsorption.

Supplementary Information The online version contains supplementary material available at <https://doi.org/10.1007/s11356-022-21176-z>.

Acknowledgements The authors are grateful to the Nanoscience and Nanotechnology Center (CNANO-UFRGS) of the Federal University of Rio Grande do Sul (UFRGS). We are also grateful to ChemAxon for giving us an academic research license for the Marvin Sketch software, Version 22.11.0 (<http://www.chemaxon.com>), 2022, used for molecule physical-chemical properties.

Author contribution Roberta A. Teixeira, investigation; Eder C. Lima, writing original draft; Antônio D. Benetti, supervising; Pascal S. Thue, conceptualization; Diana R. Lima, investigation; Farooq Sher, visualization; Glaydson S. dos Reis, reviewing and editing; Navid Rabiee, reviewing and editing; Moaaz K. Seliem, reviewing and editing; Mohamed Abatal, reviewing and editing.

Funding This study is funded by the CAPES, CNPq, and FAPERGS.

Data availability Not applicable.

Declarations

Ethics approval Not applicable.

Consent to participate The manuscript is an original work of all authors, and all authors made a significant contribution to this study.

Consent for publication The authors hereby consent to the publication of the work in the Environmental Science and Pollution Research journal.

Competing interests The authors declare no competing interests.

References

- Arefi-Oskoui S, Khataee A, Behrouz SJ, Vatanpour V, Gharamaleki SH, Orooji Y, Safarpour M (2022) Development of MoS₂/O-MWCNTs/PES blended membrane for efficient removal of dyes, antibiotics, and protein. *Sep Purif Technol* 280:1–14. <https://doi.org/10.1016/j.seppur.2021.119822>
- Arif M, Liu G, Zia urRehman M, Yousaf B, Ahmed R, Mian MM, Ashraf A, Munir MAM, Rashid MS, Naeem A (2022) Carbon dioxide activated biochar-clay mineral composite efficiently

- removes ciprofloxacin from contaminated water - reveals an incubation study. *J Clean Prod* 332:1–14. <https://doi.org/10.1016/j.jclepro.2021.130079>
- Baaloudj O, Assadi I, Nasrallah N, El-Jery A, Khezami L, Assadi AA (2021) Simultaneous removal of antibiotics and inactivation of antibiotic-resistant bacteria by photocatalysis: a review. *J Water Process Eng* 42:1–11. <https://doi.org/10.1016/j.jwpe.2021.102089>
- Bondarczuk K, Piotrowska-Seget Z (2019) Microbial diversity and antibiotic resistance in a final effluent-receiving lake. *Sci Total Environ* 650:2951–2961. <https://doi.org/10.1016/j.scitotenv.2018.10.050>
- Caicedo DF, dos Reis GS, Lima EC, de Brum IAS, Thue PS, Cazacliu BG, Lima DR, dos Santos AH, Dotto GL (2020) Efficient adsorbent based on construction and demolition wastes functionalized with 3-aminopropyltriethoxysilane (APTES) for the removal of ciprofloxacin from hospital synthetic effluents. *J Environ Chem Eng* 8:1–7. <https://doi.org/10.1016/j.jece.2020.103875>
- Çok SS, Gizli N (2020) Hydrophobic silica aerogels synthesized in ambient conditions by preserving the pore structure via two-step silylation. *Ceram Int* 46:27789–27799. <https://doi.org/10.1016/j.ceramint.2020.07.278>
- Cunha MR, Lima EC, Lima DR, da Silva RS, Thue PS, Seliem MK, Sher F, dos Reis GS, Larsson SH (2020) Removal of captopril pharmaceutical from synthetic pharmaceutical-industry wastewaters: use of activated carbon derived from *Butia catarinensis*. *J Environ Chem Eng* 8:1–9. <https://doi.org/10.1016/j.jece.2020.104506>
- de Oliveira Carvalho C, Rodrigues DLC, Lima EC, Umpierrez CS, Caicedo DF, Machado FM (2019) Kinetic, equilibrium, and thermodynamic studies on the adsorption of ciprofloxacin by activated carbon produced from Jerivá (*Syagrus Romanzoffiana*). *Environ Sci Pollut Res* 26:4690–4702. <https://doi.org/10.1007/s11356-018-3954-2>
- Desiraju GR, Ho PS, Kloos L, Legon AC, Marquardt R, Metrangolo P, Politzer P, Resnat G, Rissanen K (2013) Definition of the halogen bond (IUPAC Recommendations 2013). *Pure Appl Chem* 85:1711–1713. <https://doi.org/10.1351/PAC-REC-12-05-10>
- dos Reis GS, Sampaio CH, Lima EC, Wilhelm M (2016) Preparation of novel adsorbents based on combinations of polysiloxanes and sewage sludge to remove pharmaceuticals from aqueous solutions. *Colloids Surf a: Physicochem Eng Aspects* 497:304–315. <https://doi.org/10.1016/j.colsurfa.2016.03.021>
- dos Reis GS, Guy M, Mathieu M, Jebrane M, Lima EC, Thyrel M, Dotto GL, Larsson SH (2022) A comparative study of chemical treatment by $MgCl_2$, $ZnSO_4$, $ZnCl_2$, and KOH on physicochemical properties and acetaminophen adsorption performance of biobased porous materials from tree bark residues. *Colloids Surf a: Physicochem Eng Aspects* 642:1–13. <https://doi.org/10.1016/j.colsurfa.2022.128626>
- Foroughi M, Khiadani M, Kakhki S, Kholghi V, Naderi K, Yektay S (2022) Effect of ozonation-based disinfection methods on the removal of antibiotic-resistant bacteria and resistance genes (ARB/ARGs) in water and wastewater treatment: a systematic review. *Sci Total Environ* 811:1–23. <https://doi.org/10.1016/j.scitotenv.2021.151404>
- Goertzen SL, Theriault KD, Oickle AM, Tarasuk AC, Andreas HA (2010) Standardisation of the Boehm titration. Part I. CO₂ expulsion and endpoint determination. *Carbon* 48:1252–1261. <https://doi.org/10.1016/j.carbon.2009.11.050>
- Guellati A, Maachi R, Chaabane T, Darchen A, Danish M (2022) Aluminum dispersed bamboo activated carbon production for effective removal of Ciprofloxacin hydrochloride antibiotics: optimization and mechanism study. *J Environ Manage* 301:1–11. <https://doi.org/10.1016/j.jenvman.2021.113765>
- Guy M, Mathieu M, Anastopoulos IP, Martínez MG, Rousseau F, Dotto GL, de Oliveira HP, Lima EC, Thyrel M, Larsson SH, dos Reis GS (2022) Process parameters optimization, characterization, and application of KOH-activated Norway spruce bark graphitic biochars for efficient azo dye adsorption. *Molecules* 27:1–25. <https://doi.org/10.3390/molecules27020456>
- Hagenbuch IM, Pinckney JL (2012) Toxic effect of the combined antibiotics ciprofloxacin, lincomycin, and tylosin on two species of marine diatoms. *Water Res* 46:5028–5036. <https://doi.org/10.1016/j.watres.2012.06.040>
- Han L, Khalil AME, Wang J, Chen Y, Li F, Chang H, Zhang H, Liu X, Li G, Jia Q, Zhang S (2022) Graphene-boron nitride composite aerogel: a high-efficiency adsorbent for ciprofloxacin removal from water. *Sep Purif Technol* 278:1–9. <https://doi.org/10.1016/j.seppur.2021.119605>
- Hanafy H, Li Z, Sellaoui L, Yazidi A, Wang H, Lima EC, Cimirro NFGM, Lamine AB, Erto A (2021) Theoretical interpretation of the adsorption of amoxicillin on activated carbon via physical model. *Environ Sci Pollut Res* 28:30714–30721. <https://doi.org/10.1007/s11356-021-12696-1>
- Igwegbe CA, Oba SN, Aniagor CO, Adeniyi AG, Ighalo JO (2021) Adsorption of ciprofloxacin from water: a comprehensive review. *J Ind Eng Chem* 93:57–77. <https://doi.org/10.1016/j.jiec.2020.09.023>
- Jagiello J, Thommes M (2004) Comparison of DFT characterization methods based on N₂, Ar, CO₂, and H₂ adsorption applied to carbons with various pore size distributions. *Carbon* 42:1227–1232. <https://doi.org/10.1016/j.carbon.2004.01.022>
- Karoui S, Arfi RB, Mougin K, Ghorbal A, Assadi AA, Amrane A (2020) Synthesis of novel biocomposite powder for simultaneous removal of hazardous ciprofloxacin and methylene blue: central composite design, kinetic and isotherm studies using Brouers-Sotolongo family models. *J Hazard Mater* 387:1–17. <https://doi.org/10.1016/j.jhazmat.2019.121675>
- Khan NA, Najam T, Shah SSA, Hussain E, Ali H, Hussain S, Shaheen A, Ahmad K, Ashfaq M (2020) Development of Mn-PBA on GO sheets for adsorptive removal of ciprofloxacin from water: Kinetics, isothermal, thermodynamic, and mechanistic studies. *Mater Chem Phys* 245:1–11. <https://doi.org/10.1016/j.matchemphys.2020.122737>
- Kollarahithlu SC, Balakrishnan RM (2021) Adsorption of pharmaceuticals pollutants, ibuprofen, acetaminophen, and streptomycin from the aqueous phase using amine-functionalized superparamagnetic silica nanocomposite. *J Clean Prod* 294:1–9. <https://doi.org/10.1016/j.jclepro.2021.126155>
- Kovtun A, Campodoni E, Favaretto L, Zambianchi M, Salatino A, Amalfitano S, Navacchia ML, Casentini B, Palermo V, Sandri M, Melucci M (2020) Multifunctional graphene oxide/biopolymer composite aerogels for microcontaminants removal from drinking water. *Chemosphere* 259:1–10. <https://doi.org/10.1016/j.chemosphere.2020.127501>
- Kudo MVF, de Oliveira LLG, Suquila FAC, de Almeida FG, Segatelli MG, Lima EC, Dias SLP, Tarley CRT (2020) Performance of avocado seed activated carbon as adsorbent for highly sensitive determination of Cd using a flow injection system online coupled to TS-FF-AAS. *J Brazilian Chem Soc* 31:100–108. <https://doi.org/10.21577/0103-5053.20190132>
- Lam VT, Ngo TCQ, Bach LG (2021) Facile fabrication of novel NiFe₂O₄@Carbon composites for enhanced adsorption of emergent antibiotics. *Materials* 14:1–21. <https://doi.org/10.3390/ma14216710>
- Lawal IA, Klink M, Ndungu P (2019) Deep eutectic solvent as an efficient modifier of low-cost adsorbent for the removal of pharmaceuticals and dye. *Environ Res* 179:1–11. <https://doi.org/10.1016/j.envres.2019.108837>
- Leite AJB, Sophia AC, Thue PS, dos Reis GS, Dias SLP, Lima EC, Vaghetti JCP, Pavan FA, de Alencar WS (2017) Activated carbon from avocado seeds for the removal of phenolic compounds from

- aqueous solutions. *Desalin Water Treat* 71:168–181. <https://doi.org/10.5004/dwt.2017.20540>
- Leite AJB, Saucier C, Lima EC, dos Reis GS, Umpierrez CS, Mello BL, Shirmardi M, Dias SLP, Sampaio CH (2018) Activated carbons from avocado seed: optimization and application for removal several emerging organic compounds. *Environ Sci Pollut Res* 25:7647–7661. <https://doi.org/10.1007/s11356-017-1105-9>
- Li H, Song R, Wang Y, Zhong R, Zhang Y, Zhou J, Wang T, Zhu L (2021) Simultaneous removal of antibiotic-resistant bacteria and its resistance genes in water by plasma oxidation: Highlights the effects of inorganic ions. *Sep Purif Technol* 278:1–9. <https://doi.org/10.1016/j.seppur.2021.119672>
- Lima DR, Hosseini-Bandegharai A, Thue PS, Lima EC, de Albuquerque YRT, dos Reis GS, Umpierrez CS, Dias SLP, Tran HN (2019) Efficient acetaminophen removal from water and hospital effluents treatment by activated carbons derived from Brazil nutshells. *Colloid Surf A* 583:1–12. <https://doi.org/10.1016/j.colsurfa.2019.123966>
- Lima DR, Lima EC, Umpierrez CS, Thue PS, El-Chaghaby GA, da Silva RS, Pavan FA, Dias SP, Biron C (2019) Removal of amoxicillin from simulated hospital effluents by adsorption using activated carbons prepared from capsules of cashew of Para. *Environ Sci Pollut Res* 26:16396–16408. <https://doi.org/10.1007/s11356-019-04994-6>
- Lima EC, Hosseini-Bandegharai A, Anastopoulos I (2019c) Response to “some remarks on a critical review of the estimation of the thermodynamic parameters on adsorption equilibria. Wrong use of equilibrium constant in the van’t Hoff equation for calculation of thermodynamic parameters of adsorption - *Journal of Molecular Liquids* 273 (2019) 425–434.” *J Mol Liq* 280:298–300. <https://doi.org/10.1016/j.molliq.2019.01.160>
- Lima EC, Hosseini-Bandegharai A, Moreno-Piraján JC, Anastopoulos I (2019d) A critical review of the estimation of the thermodynamic parameters on adsorption equilibria. Wrong use of equilibrium constant in the Van’t Hoff equation for calculation of thermodynamic parameters of adsorption. *J Mol Liq* 273:425–434. <https://doi.org/10.1016/j.molliq.2018.10.048>
- Lima EC, Gomes AA, Tran HN (2020) Comparison of the nonlinear and linear forms of the van’t Hoff equation for calculation of adsorption thermodynamic parameters (ΔS° and ΔH°). *J Mol Liq* 311:1–6. <https://doi.org/10.1016/j.molliq.2020.113315>
- Lima EC, Sher F, Guleria A, Saeb MR, Anastopoulos I, Tran HN, Hosseini-Bandegharai A (2021) Is one performing the treatment data of adsorption kinetics correctly? *J Environ Chem Eng* 9:1–9. <https://doi.org/10.1016/j.jece.2020.104813>
- Lima EC, Dehghani MH, Guleria A, Sher F, Karri RR, Dotto GL, Tran HN (2021a) Adsorption: Fundamental aspects and applications of adsorption for effluent treatment. In: Dehghani MH, Karri R, Lima EC (eds.) *Green Technologies for the Defluoridation of Water*. Elsevier, pp 41–88 <https://doi.org/10.1016/b978-0-323-85768-0.00004-x>
- Ma L, Liu Y, Yang Q, Jiang L, Li G (2022) Occurrence and distribution of pharmaceuticals and personal care products (PPCPs) in wastewater-related riverbank groundwater. *Sci Total Environ* 82:1–10. <https://doi.org/10.1016/j.scitotenv.2022.153372>
- Magesh N, Annam Renita A, Siva R, Harirajan N, Santhosh A (2022) Adsorption behavior of fluoroquinolone (ciprofloxacin) using zinc oxide impregnated activated carbon prepared from jack fruit peel: kinetics and isotherm studies. *Chemosphere* 290:1–10. <https://doi.org/10.1016/j.chemosphere.2021.133227>
- Najafpoor AA, Sani ON, Alidadi H, Yazdani M, Fezabady AAN, Taghavi M (2019) Optimization of ciprofloxacin adsorption from synthetic wastewaters using γ -Al₂O₃ nanoparticles: an experimental design based on response surface methodology. *Colloid and Interface Science Communications* 33:1–7. <https://doi.org/10.1016/j.colcom.2019.100212>
- Nie XP, Liu BY, Yu HJ, Liu WQ, Yang YF (2013) Toxic effects of erythromycin, ciprofloxacin and sulfamethoxazole exposure to the antioxidant system in *Pseudokirchneriella subcapitata*. *Environ Pollut* 172:23–32. <https://doi.org/10.1016/j.envpol.2012.08.013>
- Oickle AM, Goertzen SL, Hopper KR, Abdalla YO, Andreas HA (2010) Standardisation of the Boehm titration: Part II. Method of agitation, the effect of filtering, and dilute titrant. *Carbon* 48:3313–3322. <https://doi.org/10.1016/j.carbon.2010.05.004>
- Panahi AH, Ashrafi SD, Kamani H, Khodadadi M, Lima EC, Mostafapour FK, Mahvi AH (2019) Removal of cephalixin from artificial wastewater by mesoporous silica materials using Box-Behnken response surface methodology. *Desalin Water Treat* 159:169–180. <https://doi.org/10.5004/dwt.2019.24109>
- Qiu W, Sun J, Fang M, Luo S, Tian Y, Dong P, Xu B, Zheng C (2019) Occurrence of antibiotics in the main rivers of Shenzhen, China: association with antibiotic resistance genes and microbial Community. *Sci Total Environ* 653:334–341. <https://doi.org/10.1016/j.scitotenv.2018.10.398>
- Rahman N, Varshney P (2021) Facile synthesis and characterization of Zn(II)-impregnated chitosan/graphene oxide: evaluation of its efficiency for removal of ciprofloxacin from aqueous solution. *J Inorg Organomet Polym Mater* 31:3595–3612. <https://doi.org/10.1007/s10904-021-01981-8>
- Sadredinamin M, Shabani M, Karimi A, Sohrabi MR, Karimi-Yazdi M, Ghalavand Z, Alebouyeh M (2022) Virulence genes expression profiling of different *Shigella flexneri* serotypes in response to sub-inhibitory concentrations of azithromycin and ciprofloxacin. *Gut Pathogens* 14:10. <https://doi.org/10.1186/s13099-022-00483-3>
- Sellaoui L, Mechi N, Lima EC, Dotto GL, Lamine AB (2017) Adsorption of diclofenac and nimesulide on activated carbon: statistical physics modeling and effect of adsorbate size. *J Phys Chem Solids* 109:117–123. <https://doi.org/10.1016/j.jpcs.2017.05.019>
- Sellaoui L, Kehili M, Lima EC, Thue PS, Bonilla-Petriciolet A, Lamine AB, Dotto GL, Erto A (2019) Adsorption of phenol on microwave-assisted activated carbons: ! and interpretation. *J Mol Liq* 274:309–314. <https://doi.org/10.1016/j.molliq.2018.10.098>
- Sellaoui L, Yazidi A, Taamalli A, Bonilla-Petriciolet A, Louis F, El-Bakali A, Badawi M, Lima EC, Lima DR (2021) Chen Z (2021) Adsorption of 3-aminophenol and resorcinol on avocado seed activated carbon: mathematical modelling, thermodynamic study and description of adsorbent performance. *J Mol Liq* 342:116952. <https://doi.org/10.1016/j.molliq.2021.116952>
- Sellaoui L, Dhaouadi F, Taamalli S, AlZahrani HYS, Louis F, El-Bakali A, Erto A, Lamine AB, Lima DR, Lima EC (2022) Chen Z (2022) Application of a multilayer physical model for the critical analysis of the adsorption of nicotinamide and propranolol on magnetic-activated carbon. *Environ Sci Pollut Res* 29:30184–30192. <https://doi.org/10.1007/s11356-021-18483-2>
- Sophia CA, Lima EC (2018) Removal of emerging contaminants from the environment by adsorption. *Ecotoxicol Environ Saf* 150:1–17. <https://doi.org/10.1016/j.ecoenv.2017.12.026>
- STATISTA (2020). Production of avocado in Brazil from 2013 to 2019. <https://www.statista.com/statistics/934976/brazil-avocado-production-volume/>. The website was visited on February 19th, 2022.
- Teixeira RA, Lima EC, Benetti AD, Thue PS, Cunha MR, Cimirro NFGM, Sher F, Dehghani MH, dos Reis GS, Dotto GL (2021) Preparation of hybrids of wood sawdust with 3-aminopropyltriethoxysilane. Application as an adsorbent to remove Reactive Blue 4 dye from wastewater effluents. *J Taiwan Inst Chem Eng* 125:141–152. <https://doi.org/10.1016/j.jtice.2021.06.007>
- Thommes M, Kaneko K, Neimark AV, Olivier JP, Rodriguez-Reinoso FJ, Rouquerol KS, Sing W (2015) Physisorption of gases, with special reference to the evaluation of surface area and pore size distribution (IUPAC Technical Report). *Pure Appl Chem* 87:1051–1069. <https://doi.org/10.1515/pac-2014-1117>

- Thue PS, Lima EC, Sieliechi JM, Saucier C, Dias SLP, Vaghetti JCP, Rodembusch FS, Pavan FA (2017) Effects of first-row transition metals and impregnation ratios on the physicochemical properties of microwave-assisted activated carbons from wood biomass. *J Colloid Interface Sci* 486:163–175. <https://doi.org/10.1016/j.jcis.2016.09.070>
- Thue PS, Umpierrez CS, Lima EC, Lima DR, Machado FM, dos Reis GS, da Silva RS, Pavan FA, Tran HN (2020) Single-step pyrolysis for producing magnetic activated carbon from tucumã (*Astrocaryum aculeatum*) seed and nickel(II) chloride and zinc(II) chloride. Application for removal of Nicotinamide and Propanolol. *J Hazard Mater* 398:1–13. <https://doi.org/10.1016/j.jhazmat.2020.122903>
- Tian Y, Yao S, Zhou L, Hu Y, Lei J, Wang L, Zhang J, Liu Y, Cui C (2022) Efficient removal of antibiotic-resistant bacteria and intracellular antibiotic resistance genes by heterogeneous activation of peroxymonosulfate on hierarchical macro-mesoporous Co₃O₄-SiO₂ with enhanced photogenerated charges. *J Hazard Mater* 430:1–10. <https://doi.org/10.1016/j.jhazmat.2021.127414>
- Tomul F, Arslan Y, Kabak B, Trak D, Kendüzler E, Lima EC, Tran HN (2020) Peanut shells-derived biochars prepared from different carbonization processes: comparison of characterization and mechanism of naproxen adsorption in water. *Sci Total Environ* 726:1–16. <https://doi.org/10.1016/j.scitotenv.2020.137828>
- Wamba AGN, Lima EC, Ndi SK, Thue PS, Kayem JG, Rodembusch FS, dos Reis GS, de Alencar WS (2017) Synthesis of grafted natural pozzolan with 3-aminopropyltriethoxysilane: preparation, characterization, and application for removal of Brilliant Green 1 and Reactive Black 5 from aqueous solutions. *Environ Sci Pollut Res* 24:21807–21820. <https://doi.org/10.1007/s11356-017-9825-4>
- Wang Y, Wei W, Lin Y, Zhang M, Wang Y, Liu M (2020) Assembly of SPS/MgSi assisted by dopamine with excellent removal performance for ciprofloxacin. *J Environ Sci* 94:111–118. <https://doi.org/10.1016/j.jes.2020.03.016>
- Wang Q, Yang M, Qi X, Wang J, Sun K, Li Z, Deng G (2021) A novel graphene oxide decorated with halloysite nanotubes (HNTs/GO) composite used for the removal of levofloxacin and ciprofloxacin in a wide pH range. *New J Chem* 45:1–12. <https://doi.org/10.1039/d1nj03807a>
- Wang R, Ji M, Zhai H, Guo Y, Liu Y (2021) Occurrence of antibiotics and antibiotic resistance genes in WWTP effluent-receiving water bodies and reclaimed wastewater treatment plants. *Sci Total Environ* 796:1–12. <https://doi.org/10.1016/j.scitotenv.2021.148919>
- Wu G, Ma J, Li S, Guan J, Jiang B, Wang L, Li J, Wang X, Chen L (2018) Magnetic copper-based metal-organic framework as an effective and recyclable adsorbent for removal of two fluoroquinolone antibiotics from aqueous solutions. *J Colloid Interface Sci* 528:360–371. <https://doi.org/10.1016/j.jcis.2018.05.105>
- Wu Y, Zheng H, Li H, Sun Y, Zhao C, Zhao R, Zhang C (2021) Magnetic nickel-cobalt sulfide/sodium dodecyl benzene sulfonate with excellent ciprofloxacin adsorption capacity and wide pH adaptability. *Chem Eng J* 426:1–9. <https://doi.org/10.1016/j.cej.2020.127208>
- Xikhongelo RV, Mtunzi FM, Diagboya PN, Olu-Owolabi BI, Düring RA (2021) Polyamidoamine-functionalized graphene oxide-SBA-15 mesoporous composite: adsorbent for aqueous arsenite, cadmium, ciprofloxacin, ivermectin, and tetracycline. *Ind Eng Chem Res* 60:3957–3968. <https://doi.org/10.1021/acs.iecr.0c04902>
- Yadav A, Asthana A, Singh AK, Chakraborty R, Vidya SS, Susan MABH, Carabineiro SAC (2021) Adsorption of cationic dyes, drugs, and metal from aqueous solutions using a polymer composite of magnetic/ β -cyclodextrin/activated charcoal/Na alginate: Isotherm, kinetics and regeneration studies. *J Hazard Mater* 409:1–22. <https://doi.org/10.1016/j.jhazmat.2020.124840>
- Yang Q, Yu H, He Y, Liu Z, Qin C, Liu B, Li Y (2020) Porous three-component hybrid hydrogen-bonded covalent organic polymers: design, synthesis and ciprofloxacin adsorption. *Eur Polymer J* 123:1–10. <https://doi.org/10.1016/j.eurpolymj.2019.109445>
- Yazidi A, Sellaoui L, Badawi M, Lima EC, Bonilla-Petriciolet A, Thue PS, Cimirro NFGM (2020) Lamine AB (2020) Physicochemical interpretation of the adsorption of 4-Bromophenol and 4-chloroaniline on activated carbon. *J Environ Chem Eng* 8:104542. <https://doi.org/10.1016/j.jece.2020.104542>
- Yu F, Chen D, Ma J (2018) Adsorptive removal of ciprofloxacin by ethylenediaminetetraacetic acid/ β -cyclodextrin composite from aqueous solution. *New J Chem* 42:1–8. <https://doi.org/10.1039/c7nj03770h>
- Yu D, He J, Xie T, Xu Q, Li G, Du L, Huang J, Yang J, Li W, Wang J (2022) Peroxymonosulfate activation using a composite of copper and nickel oxide coated on SBA-15 for the removal of sulfonamide antibiotics. *Environ Res* 206:1–11. <https://doi.org/10.1016/j.envres.2021.112301>

Publisher's note Springer Nature remains neutral with regard to jurisdictional claims in published maps and institutional affiliations.